*Int. J. Heat Mass Transfer.* Vol. 34, No. 7, pp. 1717–1732, 1991
Printed in Great Britain

0017–9310/91 $3.00 + 0.00


# Unidirectional solidification of a binary alloy and the effects of induced fluid motion

D. G. NEILSON and F. P. INCROPERA

Heat Transfer Laboratory, School of Mechanical Engineering, Purdue University, West Lafayette, IN 47907, U.S.A.

(*Received* 19 *June* 1990 *and in final form* 6 *August* 1990)

**Abstract**—Solidification of a binary substance in a bottom-chilled geometry is numerically simulated under conditions for which large-scale convection results from a compositionally induced density inversion in the mushy region. Model results successfully predict characteristics of mushy region channel formation which have previously been observed but have heretofore eluded prediction. Channel growth is predicted to begin at the liquidus front and, due to localized freezing point depression (melting), to propagate downward toward the chill plate. The channels act as paths of least resistance for the transport of interdendritic fluid into the overlying bulk fluid. Fluid escaping from the mushy zone forms buoyant plumes at the mouth of each channel, and the plumes are sustained by penetration of bulk liquid across the liquidus front and subsequent advection toward the channels. Predictions for channel development and flow in the overlying melt agree qualitatively with previous experimental observations.

## 1. INTRODUCTION

THE UNIDIRECTIONAL (upward) solidification of off-eutectic, binary alloys can lead to large-scale convection, even in the presence of the stabilizing, vertical temperature gradient. Segregation of the two constituents, which results from solubility constraints imposed by the alloy phase diagram, yields composition variations within the liquid phase which alter the net density distribution of the system. If the liquid within the two-phase (mushy) region is enriched by the lighter species as solid is precipitated, a density inversion is created. Such inversions are generally unstable and give rise to finger-type, double-diffusive convection [1].

Copeley *et al.* [2] were the first investigators to recognize the presence and the role of double-diffusive convection in the freezing of bottom-chilled castings. Using aqueous $NH_4Cl$, a metal analog that freezes dendritically, they were able to trace the origin of casting defects (freckles) to fluid motion induced by the density inversion. Freckles are vertically aligned regions of nearly-eutectic composition (often spanning the entire length of the casting). They are formed during phase change by fluid which ascends along preferential paths in the mushy region, melting portions of the adjoining dendritic network as it passes. The attendant formation of channels within the casting represents a severe form of macrosegregation, since the composition and crystalline structure of solid which ultimately forms within the channels differs significantly from that of nearby solid. Moreover, plumes that issue from channels during solidification advect interdendritic fluid of different composition into the upper region of the melt. Normal segregation is thereby associated with dilution or enrichment of the bulk liquid such that, upon complete solidification, the composition of the casting varies from bottom to top. Convective instability leading to freckle formation in bottom-chilled castings has also been experimentally investigated by McCay *et al.* [3]. Visualization of the flow field prior to plume development revealed undulations and periodic roll cells in the fluid just above the liquidus, which were considered to be a solutal analog to manifestations of the classic Rayleigh–Bénard instability. Thus, it is now accepted that freckles and normal macrosegregation in metal alloys [4–7] are unequivocably linked to gravitationally induced thermosolutal convection.

Because compositional inhomogeneity significantly diminishes the quality of castings, means to offset the naturally induced fluid motion have been investigated. Using the aqueous $NH_4Cl$ model alloy, Sample and Hellawell [8, 9] employed a novel mold rotation/precession technique to alter the orientation of the gravitational vector relative to the freezing surface. Although their original hypothesis was that mold movement would inhibit channel formation by preventing sustained fluid flow in a single direction, they ultimately concluded that the observed decrease in freckles was due to a translation of bulk liquid across the liquidus front. The genesis of channels was also examined, and it was determined that withdrawal of bulk liquid near the liquidus interface quickly led to the development of a freckle, while punctures in the growth front failed to propagate and were ultimately overgrown by the adjoining dendritic network. They concluded, therefore, that freckle nucleation occurred at the growth front and that the concomitant plume which develops leads to backward propagation of the channel toward the freezing surface. In an extension of this work, Sarazin and Hellawell [10] developed an expression for the effective critical Rayleigh number, $Ra_{\text{eff}}$, using the primary interdendritic spacing as a

## NOMENCLATURE

| | |
|---|---|
| $c$ | specific heat |
| $\mathscr{D}$ | binary mass diffusivity |
| $f$ | mass fraction |
| $\bar{f}_s$ | total fraction of solid |
| $g$ | volume fraction |
| $g$ | gravitational acceleration |
| $h$ | enthalpy |
| $H$ | mold height |
| $k$ | thermal conductivity |
| $Le$ | Lewis number |
| $P$ | pressure |
| $q$ | heat rate |
| $Ra$ | Rayleigh number |
| $r_o$ | outer radius |
| $t$ | time |
| $T$ | temperature |
| $u, v$ | $z$-, $r$-direction velocity components |
| $\mathbf{V}$ | velocity vector |
| $z, r$ | axial and radial coordinates. |

Greek symbols

| | |
|---|---|
| $\beta_S$ | solutal expansion coefficient |
| $\beta_T$ | thermal expansion coefficient |
| $\kappa$ | permeability |
| $\kappa_o$ | permeability coefficient |
| $\mu$ | dynamic viscosity |
| $\rho$ | density |
| $\psi$ | stream function. |

Subscripts

| | |
|---|---|
| c | cold boundary |
| e | eutectic |
| eff | effective |
| f | fusion |
| l | liquid |
| liq | liquidus |
| o | initial |
| oc | initial temperature relative to cold boundary |
| ol | initial temperature relative to liquidus temperature |
| s | solid. |

Superscript

| | |
|---|---|
| $\alpha$ | constituent of binary mixture. |

length scale. Agreement between values of $Ra_{eff}$ for the aqueous model alloy and metal systems was good, even though the dendritic spacing and material properties for the two systems differ significantly.

Perhaps the most promising means for reducing macrosegregation in small specialty castings or crystals involves solidification under low-gravity conditions. McCay and McCay [11] performed a series of experiments in an alternating increasing–decreasing $g$ field (produced by parabolic trajectories in an aircraft) and showed that plumes issuing from a solidifying aqueous alloy were completely suppressed during low-$g$ conditions.

Morphological and hydrodynamic instabilities associated with a unidirectionally solidified alloy have been analyzed [12, 13]. While such analyses are useful for determining conditions leading to instability (e.g. values of critical thermal or solutal Rayleigh numbers), detailed transport phenomena associated with the phase change process cannot be predicted. For example, the evolution of freckles and their effect on fluid motion are not revealed in such analyses. To obtain such detail, recourse must be made to more comprehensive models designed to capture the complicated interactions between momentum, energy and species transfer in the mushy and melt regions.

Recently, continuum models based on volume-averaging techniques [14, 15] have yielded generalized forms of mass, momentum, energy and species conservation equations which are sufficiently robust to treat the many complexities associated with multi-component phase change. Such formulations eliminate the need for explicit consideration of interface (solidus and liquidus) motion or for coupling boundary conditions internal to the domain. Simulations for simple two-dimensional geometries have successfully predicted the effect of interdendritic fluid flow on the development of segregates, remelting due to liquidus temperature depression, double-diffusive layering in the melt region, and liquidus front irregularities, as well as the coupling between convection in the melt and mushy regions [15–17].

Because details associated with freckle nucleation and evolution are not fully understood, the objective of this work has been to numerically simulate bottom-chilled casting for conditions known to exhibit pronounced freckle formation. In this manner, questions concerning the influence of transport phenomena during and after freckle development can be assessed. For example, how and where do mushy zone channels form and what sustains or eliminates their existence? Ultimately, insights gained by such a study may lead to procedures for minimizing freckle formation.

## 2. MATHEMATICAL MODEL

Solidification of a binary solution has been simulated for a cylindrical, axisymmetric cavity which is chilled from below. The assumption of two-dimensionality is not entirely consistent with observations of the channels/freckles [2, 8, 9], which are best characterized as discrete sites generally distributed in a

seemingly random pattern across the liquidus front. Nevertheless, a two-dimensional model may be expected to reveal key features of the solidification process. The continuum conservation equations for mass, momentum, energy and species may be expressed, respectively, as

$$\frac{\partial}{\partial t}(\rho)+\nabla\cdot(\rho\mathbf{V})=0 \tag{1}$$

$$\frac{\partial}{\partial t}(\rho u)+\nabla\cdot(\rho\mathbf{V}u)=\nabla\cdot(\mu_l\nabla u)-\frac{\mu_l}{\kappa}u-\frac{\partial p}{\partial z}+\rho g[\beta_T(T-T_o)+\beta_S(f_l^z-f_{l,o}^z)] \tag{2}$$

$$\frac{\partial}{\partial t}(\rho v)+\nabla\cdot(\rho\mathbf{V}v)=\nabla\cdot(\mu_l\nabla v)-\frac{\mu_l}{\kappa}v-\frac{\partial p}{\partial r}-\frac{\mu_l}{r^2}v \tag{3}$$

$$\frac{\partial}{\partial t}(\rho h)+\nabla\cdot(\rho\mathbf{V}h)=\nabla\cdot\left(\frac{k}{c_s}\nabla h\right)+\nabla\cdot\left(\frac{k}{c_s}(h_s-h)\right)-\nabla\cdot(\rho f_s(h_l-h_s)\mathbf{V}) \tag{4}$$

$$\frac{\partial}{\partial t}(\rho f^z)+\nabla\cdot(\rho\mathbf{V}f^z)=\nabla\cdot(\rho\mathscr{D}\nabla f^z)+\nabla\cdot(\rho\mathscr{D}\nabla(f_l^z-f^z))-\nabla\cdot(\rho f_s(f_l^z-f_s^z)\mathbf{V}) \tag{5}$$

where $\alpha$ refers to one of the two components in the binary mixture and a stationary (i.e. nontranslating) solid phase is assumed. Mean mixture theory is used to define the continuum density, velocity, enthalpy and species mass fraction appearing in equations (1)–(5). These definitions, the simplifying assumptions invoked during derivation of equations (1)–(5), and details associated with development of closure relationships based on the equilibrium phase diagram may be found elsewhere [14, 18].

The permeability used in equations (2) and (3) represents the only direct link between microscopic morphology and the macroscopic conservation equations. Unfortunately, there is considerable uncertainty in the dependence of $\kappa$ on parameters such as local solidification rate, liquid volume fraction, and primary/secondary dendrite arm spacing (DAS). Moreover, the directional (anisotropic) behavior of $\kappa$ is not known. One simple model for $\kappa$, which has been utilized in other computational studies [17, 19], is the empirical Blake–Kozeny expression

$$\kappa=\kappa_o\frac{g_l^3}{(1-g_l)^2} \tag{6}$$

where $\kappa_o$ is a constant based on the geometry of the flow obstruction and may be related to DAS. Assuming a value of 100 $\mu$m for DAS, $\kappa_o$ becomes $5.556\times10^{-11}$ m$^2$ [19], which is the value employed in the afore-mentioned studies. However, there is much latitude in the selection of DAS, since its value varies according to local solidification conditions and hence is not constant during solidification. It is therefore reasonable to base $\kappa_o$ on some mean value of DAS associated with the solidification process. Experiments, which used films of aqueous $NH_4Cl$ solution placed between microscope slides, revealed that DAS for this model alloy could be less than the assumed value of 100 $\mu$m. Photographs of dendritic structure showing an array of solid crystals, Fig. 1(a), and a single primary dendrite with secondary and tertiary arms, Fig. 1(b), may be utilized to infer approximate values of DAS. For a measured value of DAS = 32 $\mu$m, the value of $\kappa_o$ is reduced by an order of magnitude.

The spatially-elliptic, temporally-parabolic equations (1)–(5) were solved using a control-volume based, finite-difference scheme [20]. Since it was anticipated that predicted results would be very sensitive to the permeability, two sets of calculations were made: Case 1 (DAS = 100 $\mu$m, $\kappa_o = 5.556\times10^{-11}$ m$^2$) and Case 2 (DAS = 32 $\mu$m, $\kappa_o = 5.556\times10^{-12}$ m$^2$). The transient calculations employed a conservative time step of 1 s for the entire 35 min length of both simulations, which were performed using Gould NP/1, Cyber 205 and ETA10 computers. Choosing a mold geometry which is representative of a moderately sized casting ($H$ = 102 mm, $r_o$ = 64 mm), computational grid studies revealed that a $66\times66$ biased grid (Fig. 2) provided sufficient detail to resolve key features of the simulated process. No-slip conditions were imposed at the bottom and the vertical outer wall, while shear-free conditions were assumed at a free air/liquid interface. The top surface and the sidewall were assumed to be adiabatic, while the bottom wall was maintained isothermal at a chill plate temperature $T_c$. The centerline was treated as a line of symmetry, while all boundaries were treated as impermeable to mass transfer. Simulation of the phase change process was initiated with a superheated $NH_4Cl$ solution of uniform temperature, $T_o$, and composition, $f_o^{NH_4Cl}$. Thermophysical properties for this dendritic metal model alloy may be found in the literature [10, 17]. However, it should be noted that a value of 2.7 W m$^{-1}$ K$^{-1}$ was utilized for the solid phase thermal conductivity, $k_s$. This value was obtained from more reliable data [21] and differs considerably from that used in earlier studies.

## 3. RESULTS

The freckling potential expression [2] was utilized as a guideline for selecting initial and boundary conditions that would promote significant channel formation. These conditions are summarized in Fig. 3, which is the equilibrium phase diagram for the $NH_4Cl$–$H_2O$ system. The initial composition of aqueous $NH_4Cl$ was chosen to insure extensive mushy region growth ($f_o^{NH_4Cl} = 0.32$). Moreover, since rapid solidification minimizes or delays the onset of freckle development [6], the modelled phase change was limited to that which occurs over the extended freezing

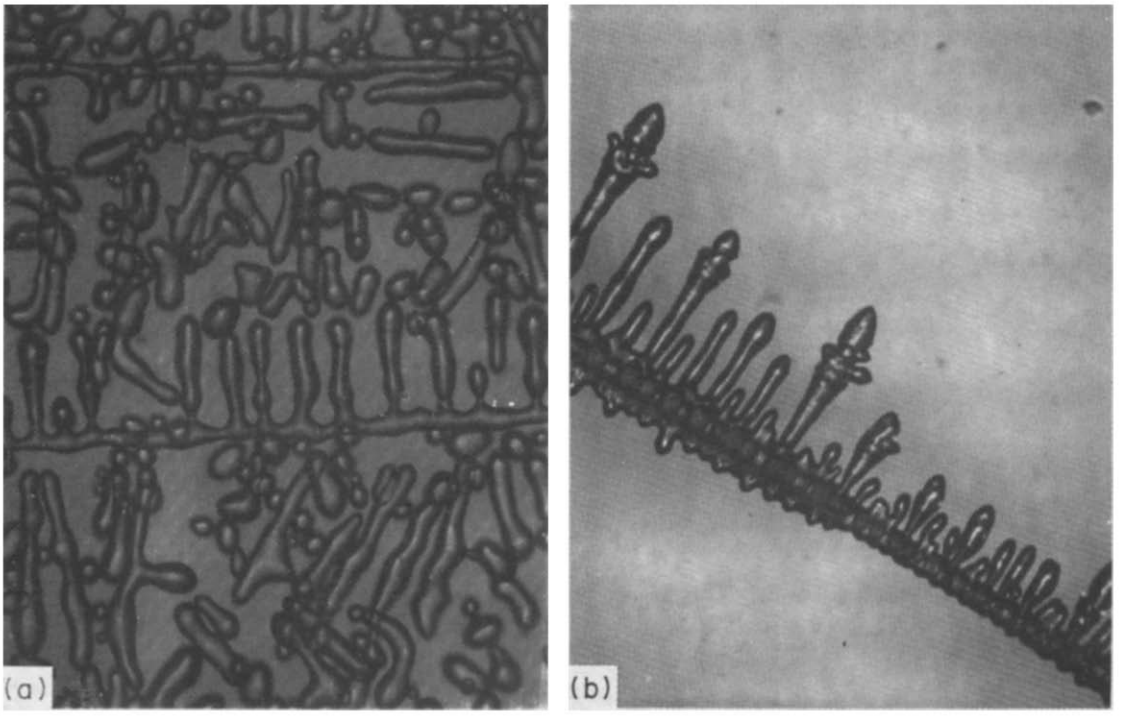


FIG. 1. Dendritic structure for aqueous $NH_4Cl$ solution: (a) multi-dendrite region; (b) single dendrite. Magnification 100 times.

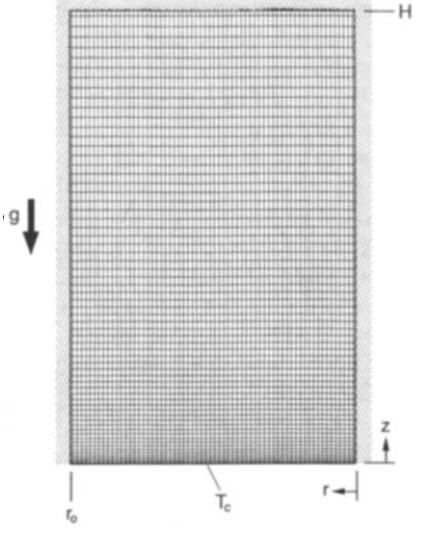


FIG. 2. Schematic of the physical system and computational domain.

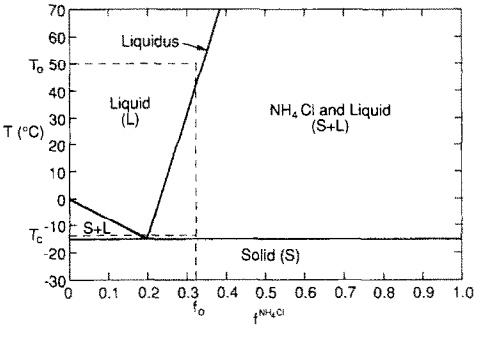


FIG. 3. Equilibrium phase diagram for $NH_4Cl$–$H_2O$ with initial and boundary conditions noted.

range but does not include the eutectic reaction ($T_c = -14°C > T_e = -15.4°C$). A slight superheat above the initial liquidus temperature ($T_{liq} = 42°C$) was used ($\Delta T_{ol} = 8°C$), while the superheat above the chill plate temperature, $\Delta T_{oc}$, was approximately 64°C.

### 3.1. *Case* 1 ($\kappa_o = 5.556 \times 10^{-11}$ m$^2$)

Predictions during the very early stages of solidification revealed no fluid motion. However, after approximately 1 min, the induced density inversion resulting from water enrichment of the liquid due to precipitation of $NH_4Cl$ solid (dendritic crystals) became unstable and fluid motion was initiated. Motion began in regions of the mushy zone adjacent to the centerline and outer wall and was created by perturbations in the permeability along the liquidus front. Such slight variations in the flow resistance of the mushy zone are manifestations of perturbed field variables (e.g. temperature), which are directly related

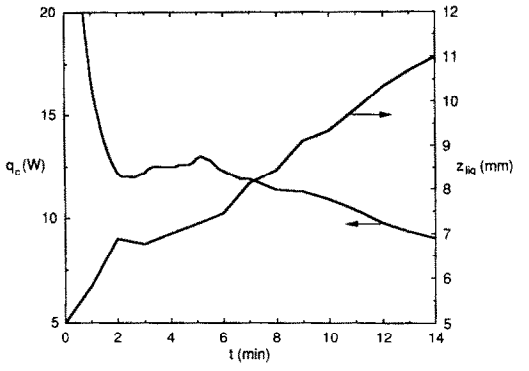


FIG. 4. Predicted heat extraction rate, $q_c$, and mean liquidus front position, $z_{liq}$, as functions of time for Case 1.

to the local volume fraction, $g_l$, used in the determination of $\kappa$. This perturbation sequence was first suggested by Sample and Hellawell [9] as a necessary condition leading to the nucleation of a channel.

Plots of heat extraction at the chilled boundary and the mean liquidus front position during the initial transient (Fig. 4) can be used to infer the onset of fluid motion. During the first 2 min, $q_c$ ($z_{liq}$) decreases (increases) in a manner which is characteristic of diffusion-dominated phase change. However, for $2 \leqslant t \leqslant 6$ min, $q_c$ increases with increasing $t$, while $z_{liq}$ decreases slightly and then continues to increase. The sudden change of slope of $q_c$ at $t \approx 2$ min is indicative of heat transfer enhancement due to the onset of advection within the mushy zone. Warm fluid from the overlying bulk liquid penetrates the mushy region, temporarily retarding liquidus front growth, to sustain the upflow of escaping interdendritic liquid. Because its effect on heat extraction is not realized until sufficient penetration has occurred, this motion begins before its influence is manifested by the results of Fig. 4.

Isotherms and liquidus front morphologies for selected times during the first 2.5 min of solidification are presented in Fig. 5. Only the lower one-third of the calculation domain is shown. Waviness in the isotherms begins near the liquidus front and the vertical surfaces, Fig. 5(a), and propagates inward and

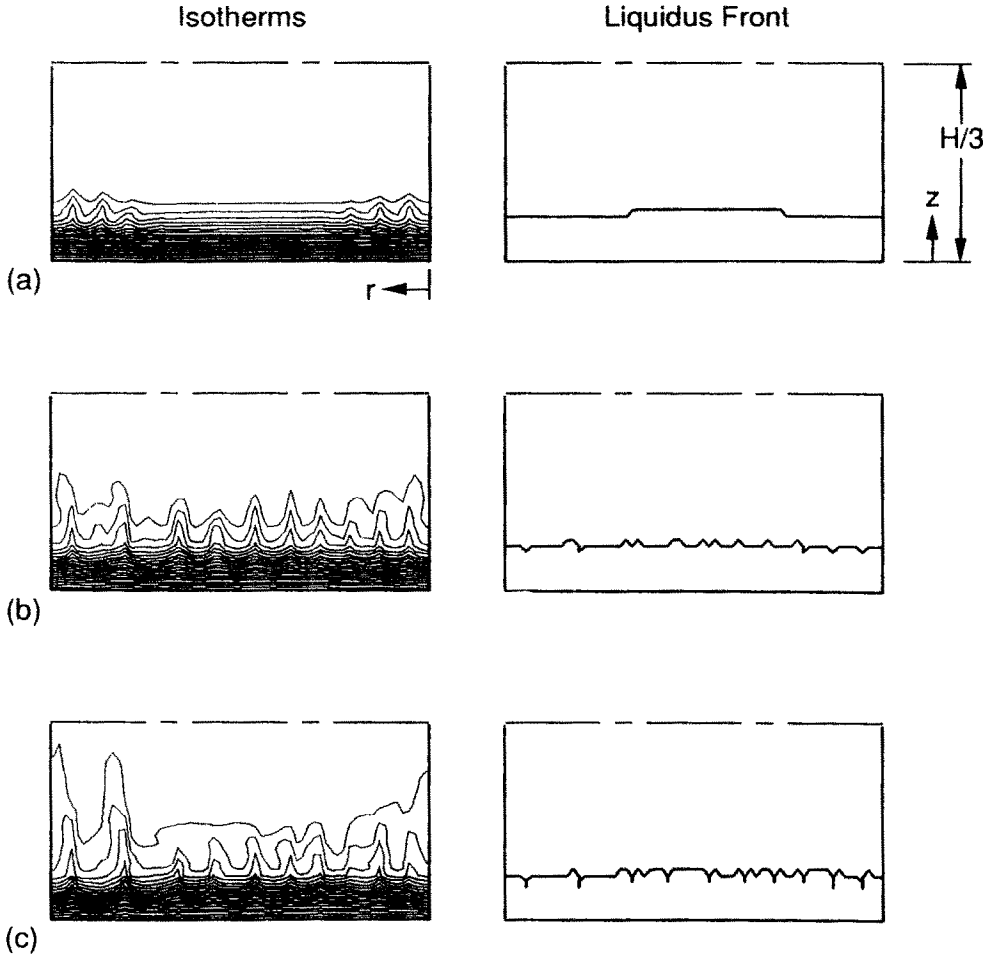


FIG. 5. Predicted isotherms and liquidus fronts for Case 1: (a) $t = 1.5$ min, $T_{min} = -14°C$, $T_{max} = 50°C$, $\bar{f}_s = 0.54\%$; (b) $t = 2$ min, $T_{min} = -14°C$, $T_{max} = 50°C$, $\bar{f}_s = 0.63\%$; (c) $t = 2.5$ min, $T_{min} = -14°C$, $T_{max} = 50°C$, $\bar{f}_s = 0.72\%$.

outward from the vertical surfaces with increasing time, Figs. 5(b) and (c). Irregularities in the growth rate of the liquidus front are predicted for $t = 1.5$ and 2 min, Figs. 5(a) and (b), and are precursors to a more distorted front and the development of channels. At $t = 2.5$ min, Fig. 5(c), ten small channels have formed due to remelting resulting from localized reductions in the liquidus temperature (i.e. a freezing point depression). Channel nucleation along the liquidus front correlates with localized water enriched, cold spots produced by ascending mushy region fluid.

Conditions following the onset of liquidus front irregularities are characterized by continued formation of mushy region solid, a decrease in the number of channels, and large scale fluid motion throughout the bulk liquid. Velocity vectors, streamlines, isotherms, and contours of liquid composition (isocomps) are shown in Fig. 6 for $t = 10$ min. The liqui-

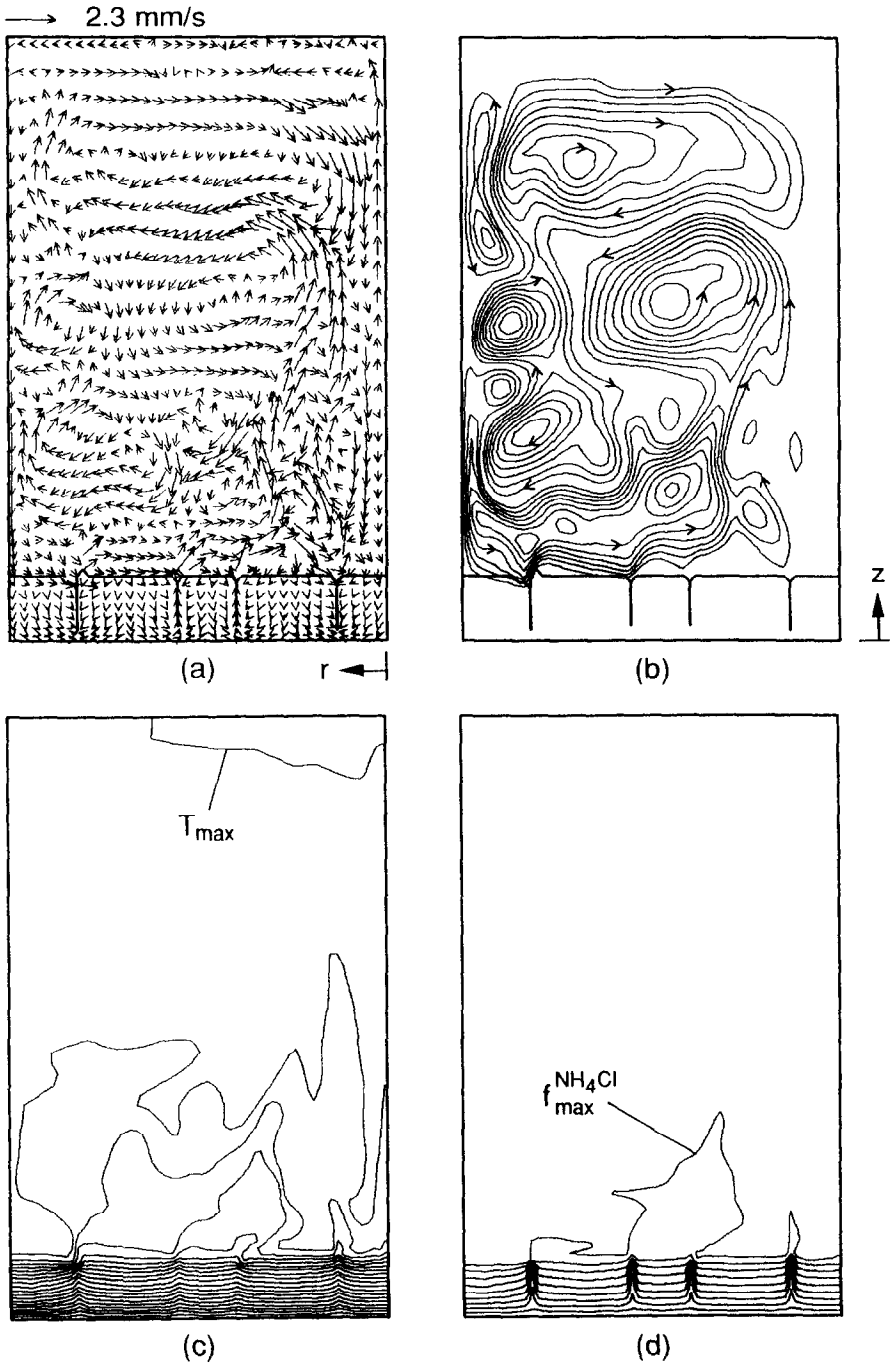


FIG. 6. Predicted solidification behavior at $t = 10$ min for Case 1: (a) velocity vectors ($|v_{max}| = 2.3$ mm s$^{-1}$); (b) streamlines; (c) isotherms ($T_{min} = -14$°C, $T_{max} = 46.8$°C); (d) liquid isocompositions ($f^{NH_4Cl}_{l,min} = 20\%$, $f^{NH_4Cl}_{l,max} = 31.5\%$).

dus front has been superimposed on the velocity vector and streamline plots, and to identify individual velocity vectors, every other vector associated with a control volume is plotted. Vigorous expulsion of interdendritic fluid is predicted to occur at each channel along the liquidus front, causing a complex multicellular flow pattern to develop in the melt. The streamlines, Fig. 6(b), reveal that mushy zone fluid emerging from the outermost channels is swept radially inward until interactions with fluid emerging from the inner channels results in an ascending plume. The width of each channel is equal to the spacing between two radial grid lines (i.e. a control volume thickness) which is 0.98 mm. Therefore, predicted channel dimensions are not independent of the finite difference mesh.

The complicated flow field in the liquid region contrasts with that of the mushy zone where fluid motion is more organized. Fluid from the overlying melt penetrates the liquidus front and enters the mushy region to sustain the outflow of interdendritic fluid at each channel. Excluding the channels and their near field, all velocity vectors in the mushy region possess a downward component of motion. However, flow velocities in the mushy region are typically 2–3 orders of magnitude less than those in the bulk liquid. Surrounding each channel, there is a well defined flow field in which the downward moving liquid simultaneously migrates toward the channel. Since the permeability is greater near each channel, a path of least resistance is provided for the migrating interdendritic fluid.

Isotherms and liquid composition contours at $t = 10$ min are shown in Figs. 6(c) and (d). The largest thermal and solutal gradients are adjacent to the cold boundary and are confined to the mushy region. More uniform conditions exist in the bulk liquid, where buoyancy induced mixing reduces nonuniformities in temperature and composition. The locations of the four channels are clearly revealed by spikes in the otherwise nearly horizontal isotherms and liquid isocompositions. These deviations are directly linked to the freckling phenomenon. The channels which develop at the liquidus front and grow downward through the mush toward the chill surface represent sites of localized freezing point depression resulting from the solubility constraints of the precipitated solid. As colder, $NH_4Cl$-depleted liquid, which is formed upon phase change, is displaced upward into warmer, solute-rich regions, it acquires energy far more readily than it acquires $NH_4Cl$ ($Le \gg 1$). Hence, the solute-depleted fluid warms, making it more resistant to freezing. The existence of such behavior at discrete radial locations is indicative of inhomogeneities in the mush (e.g. permeability) which lead to preferred flow paths. From mass continuity, fluid escaping the mushy zone along these paths must be replenished by the overlying bulk liquid.

Mechanisms associated with the closure of a channel may be delineated by examining velocity vectors and liquid isocomps corresponding to the time interval $17 \leqslant t \leqslant 18$ min, which are shown in Fig. 7 for the bottom half of the domain. At earlier times, as for example, $t = 10$ min, Fig. 6(a), interdendritic fluid feeds the second channel from the centerline by entering along the entire length of the channel, including the base region. At $t = 17$ min, Fig. 7(a), however, mushy zone fluid at the base of this channel is beginning to bypass the channel in favor of migration to neighboring channels. Thirty seconds later, Fig. 7(b), there is actually *downflow* in the second channel from the centerline and solidification near the liquidus front has promoted blockage within the channel. By $t = 18$ min, Fig. 7(c), the site of the formerly all-liquid channel is composed of mush, and the downflow of interdendritic fluid in this region is split to feed the adjoining channels. Closure of a channel is a natural consequence of the freezing process. As solidification proceeds, its rate diminishes thereby slowing the generation of lighter fluid and reducing the driving potential for fluid motion. The driving potential also decreases because the composition of the bulk liquid approaches that of the mushy region and the initial superheat dissipates. Such conditions lead to competition among the channels for the descending bulk liquid which sustains the channel plumes. This premise is supported by the liquid isocomp variations. As revealed by Fig. 7(a), upflow within each channel results in highly concentrated gradients of $NH_4Cl$. However, at this time and 30 s later, Fig. 7(b), liquid composition gradients within and around the dying channel are not as large as those at neighboring sites. As the gradients diminish, the freezing point depression decreases, rendering solidification more likely. Because the gradient is smallest near the liquidus front, channel closure begins in this region. Vestiges of the channel persist at $t = 18$ min, as revealed by localized $NH_4Cl$ enrichment at the former site of the channel, Fig. 7(c). The termination of a channel, as revealed by etched freckles in completely solidified castings, has been noted by others [4].

Conditions at $t = 19$ min are shown in Fig. 8. The most obvious difference from earlier predictions is the afore-mentioned decrease in the number of channels within the mush and the increased distortion of the liquidus front, Fig. 8(b). The velocity field, Fig. 8(a), reveals that fluid which issues from the innermost and middle channels ascends through much of the melt as buoyant plumes. The isotherms, Fig. 8(c), and liquid isocomps, Fig. 8(d), associated with the plumes clearly show that thermal and solutal penetrations into the bulk liquid are extensive. Such behavior is consistent with previous experimental observations [2, 22]. The plume rising from the outermost channel encounters recirculation cells near the channel opening which limit its vertical penetration in the melt. The isotherms also highlight the flow reversal associated with channel closure. As noted earlier, temperature contours bend upward at (active) channel sites. However, near the former location of the channel, the isotherms bend

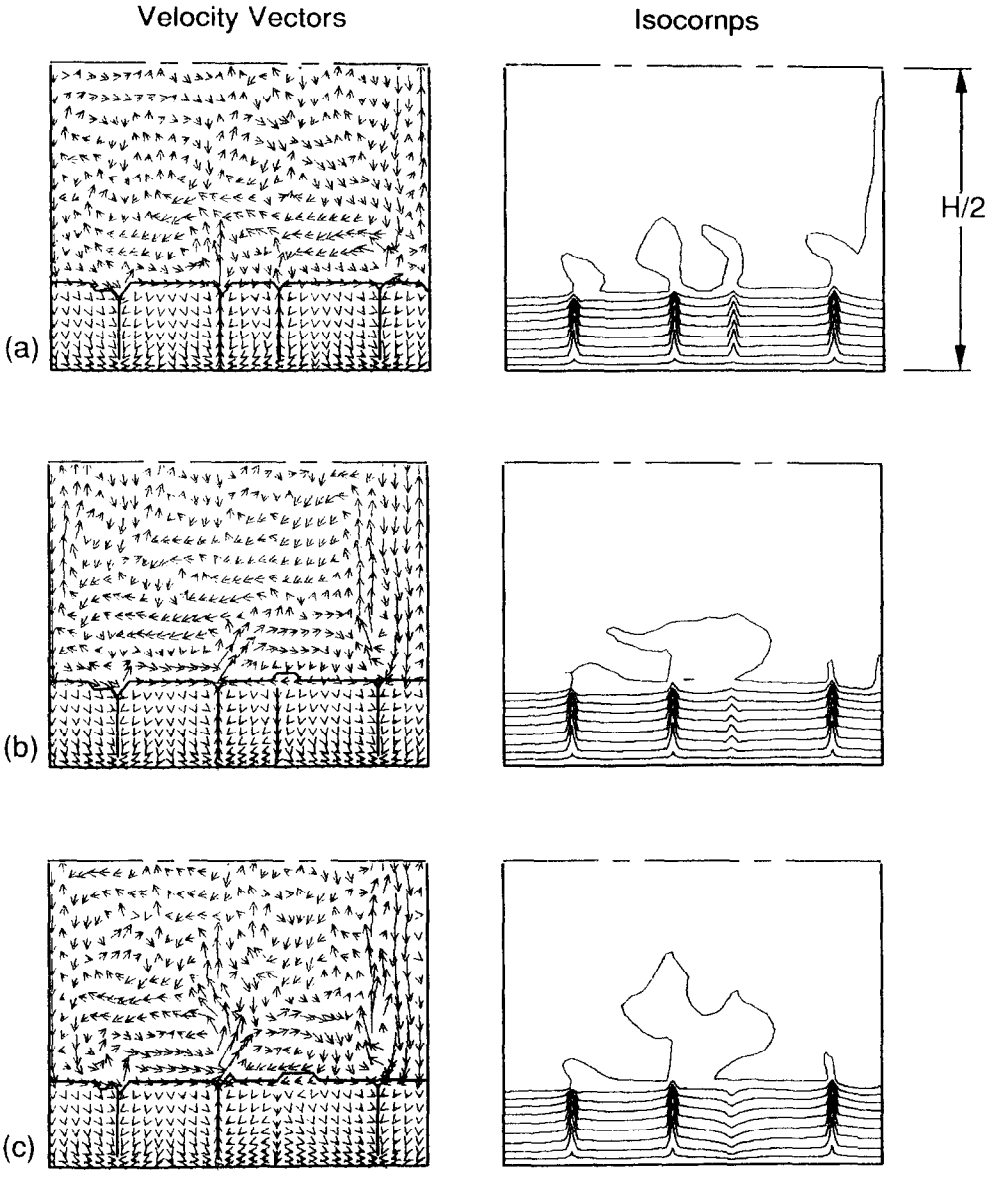


FIG. 7. Predicted dynamics of channel closing for Case 1: (a) $t = 17$ min, $|v_{max}| = 3.8$ mm s$^{-1}$, $f_{Lmin}^{NH_4Cl} = 20\%$, $f_{Lmax}^{NH_4Cl} = 30.8\%$; (b) $t = 17.5$ min, $|v_{max}| = 3.5$ mm s$^{-1}$, $f_{Lmin}^{NH_4Cl} = 20\%$, $f_{Lmax}^{NH_4Cl} = 30.8\%$; (c) $t = 18$ min, $|v_{max}| = 2.8$ mm s$^{-1}$, $f_{Lmin}^{NH_4Cl} = 20\%$, $f_{Lmax}^{NH_4Cl} = 30.8\%$.

downward, implying localized warming. Undoubtedly, the favorable permeability field associated with this region provides a convenient flow path for warm bulk liquid to intrude into the mushy zone. Liquid isocomps in Fig. 8(d) confirm the intrusion of warm, $NH_4Cl$-rich fluid.

After 35 min of solidification, the mushy zone fills approximately 20% of the cavity, even though the total fraction of solid formed, $\bar{f}_s$, is only 4.8%. Hence the aqueous solution yields a very porous dendritic network, which may be unlike some metals [10]. Three channels are still active and the liquidus front is nearly planar, Fig. 9(a). The flow field in the bulk liquid continues to be dominated by buoyant plumes and their resultant shear/buoyancy induced recirculations. Flow conditions within the mush are similar to those at earlier times, with downflow in regions removed from the channels and *seepage* toward the channels for nearby locations. The maximum temperature at this time, Fig. 9(c), is lower than the initial liquidus temperature. Correspondingly, the maximum $NH_4Cl$ liquid composition is less than the initial value, Fig. 9(d). This result further illustrates, but on a macroscopic scale, the freezing point depression created by the segregation of binary components during phase change. As solidification proceeds, the average bulk liquid composition approaches the value associated with the chill plate temperature (provided that fluid

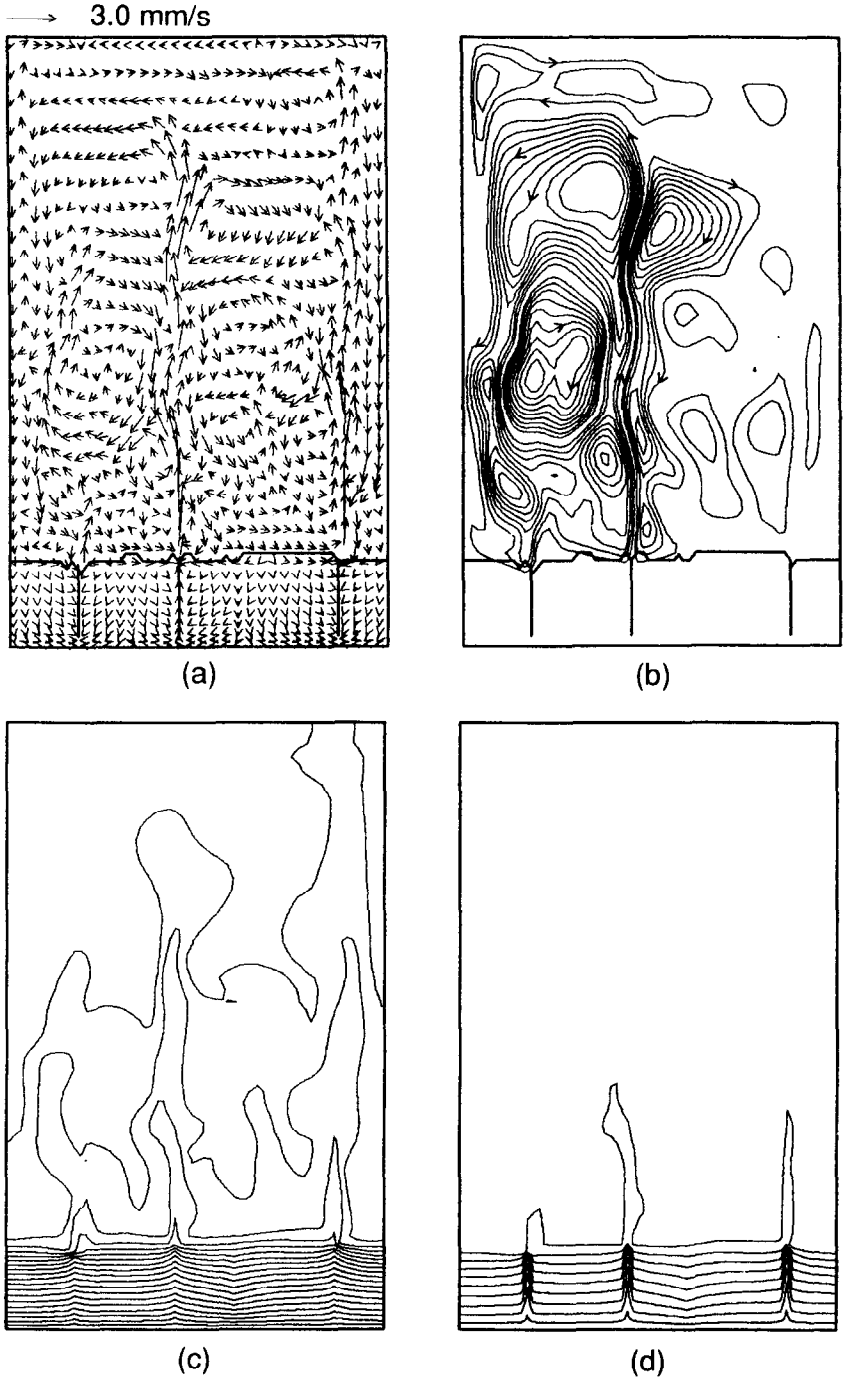


FIG. 8. Predicted solidification behavior at $t = 19$ min for Case 1: (a) velocity vectors ($|v_{max}| = 3.0$ mm s$^{-1}$); (b) streamlines; (c) isotherms ($T_{min} = -14$°C, $T_{max} = 43.1$°C); (d) liquid isocompositions ($f_{l,min}^{NH_4Cl} = 20\%$, $f_{l,max}^{NH_4Cl} = 30.7\%$).

motion results from an unstable density gradient and that solute-deficient fluid is advected upward). Hence, aside from local variations in the composition near channels, there is a global variation in liquid composition from the bottom to the top of the domain. That is, if the system were instantaneously solidified (quenched), the composition field would effectively be *locked* in place, yielding a casting with negative segregates (water-rich freckles) and macrosegregation.

### 3.2. *Case* 2 ($\kappa_o = 5.556 \times 10^{-12}$ m$^2$)

Although qualitatively similar to Case 1 predictions, the decrease in permeability (for a given $g_l$) associated with Case 2 revealed the acute sensitivity

of model predictions to this parameter. For example, both cases predicted onset of fluid motion to occur at the liquidus front after an initial diffusion-dominated transient. However, enhanced viscous damping within the mushy zone for Case 2 substantially delayed the instability and therefore prolonged the length of time in which phase change was governed by diffusion. Pronounced features of the phase change phenomena for Case 2 were, in general, less dynamic than those of Case 1.

Streamlines for selected times during the development of fluid motion are shown in Fig. 10. Predicted fluid flow, which begins at approximately $t = 5$ min, occurs along the liquidus front and is manifested by multiple, counter-rotating cells, Fig. 10(a), which increase in strength by three orders of magnitude during

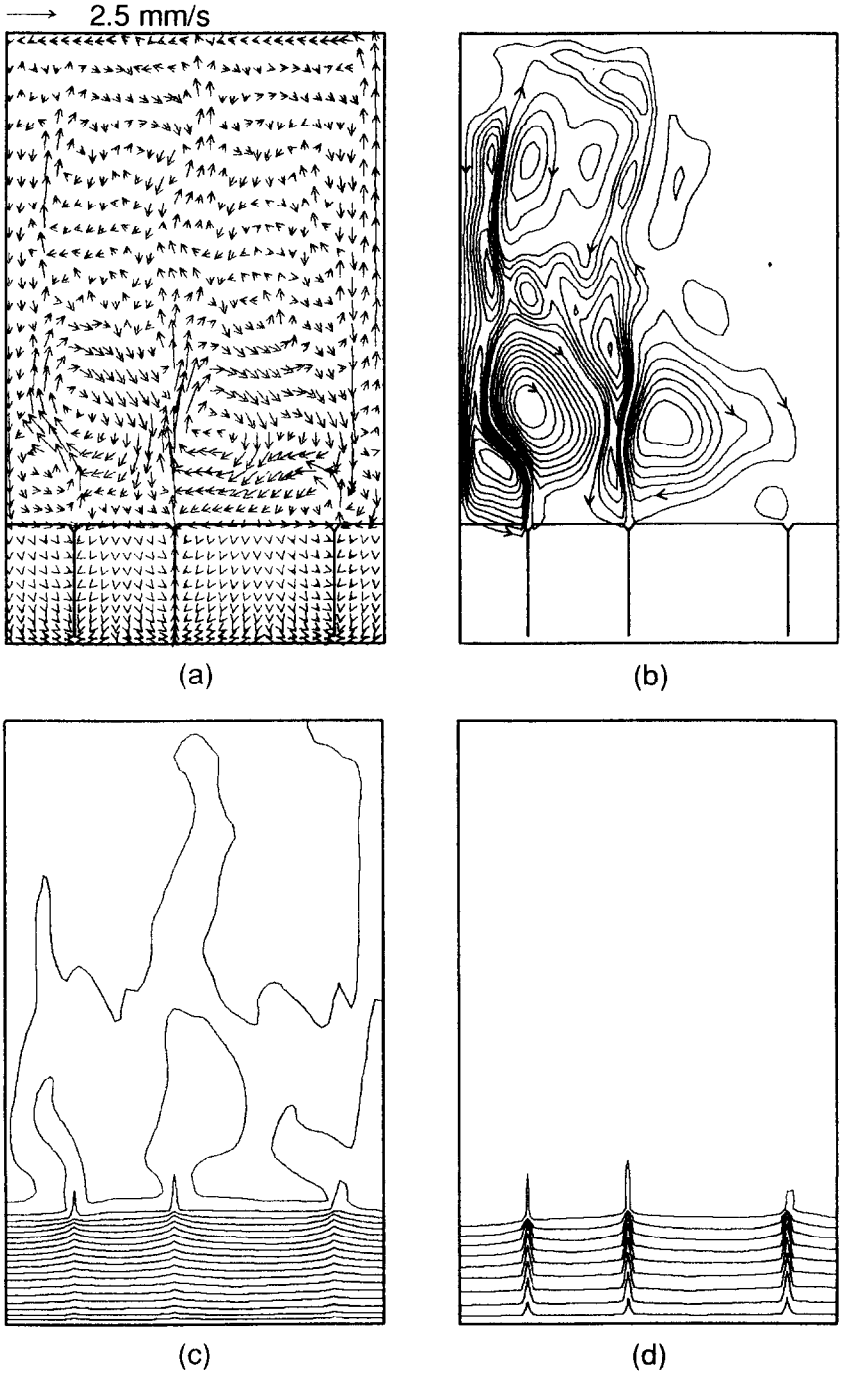


FIG. 9. Predicted solidification behavior at $t = 35$ min for Case 1: (a) velocity vectors ($|v_{max}| = 2.5$ mm s$^{-1}$); (b) streamlines; (c) isotherms ($T_{min} = -14$ C, $T_{max} = 36.3$ C); (d) liquid isocompositions ($f_{l,min}^{NH_4Cl} = 20\%$, $f_{l,max}^{NH_4Cl} = 29.6\%$).

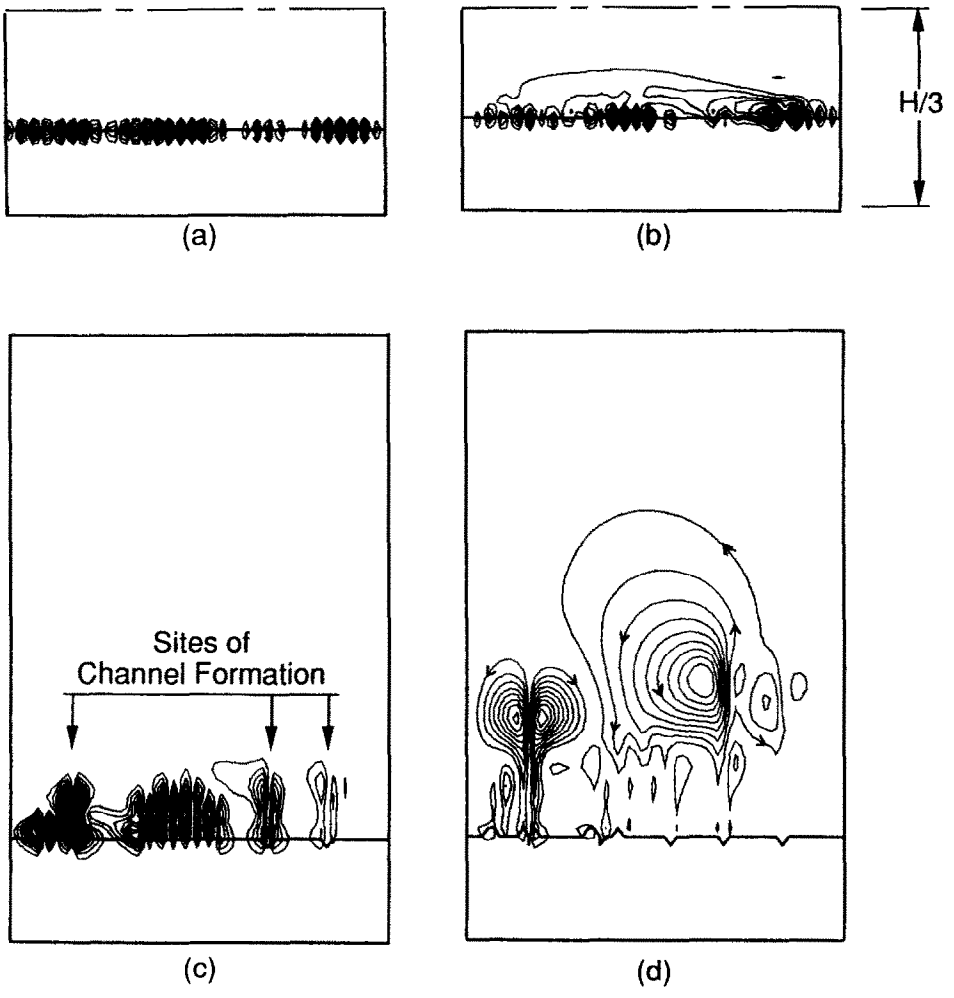


FIG. 10. Predicted streamlines for Case 2 at times of: (a) $t = 5$ min; (b) $t = 6$ min; (c) $t = 7$ min; (d) $t = 7.5$ min.

the subsequent minute, Fig. 10(b). From $t = 6$ to 7 min, nonuniformity in localized solid formation rates produces an irregular liquidus interface. At $t = 7$ min, Fig. 10(c), only three sites remain from the approximately eleven locations that initially developed. These sites, and two more that form during the following 30 s, yield the five channel nucleation sites shown in Fig. 10(d). The transition of the flow field from roll cells confined to the liquidus interface, Fig. 10(a), to discrete plumes which issue into the bulk liquid, Fig. 10(d), is revealed by conditions at the outermost channel.

Conditions after 10 min, Fig. 11, may be contrasted with those for Case 1 in Fig. 6. At this time, five channels, which extend downward by a distance which is less than 15% of the total mushy zone thickness, are predicted for Case 2, Fig. 11(a), while for the more permeable mushy region of Case 1, Fig. 6(a), four channels are predicted to penetrate from the liquidus to nearly the bottom surface. Although both flow fields are of comparable strength, the earlier onset of fluid motion calculated for Case 1 yields enhanced interchange of interdendritic and bulk liquid, thereby reducing formation of solid. That is, because the less permeable mushy zone of Case 2 inhibits the escape of interdendritic fluid and penetration of the overlying melt, sensible energy transfer is larger for Case 1 than Case 2. Downward propagation of the channels is evident, Fig. 11(b), but the remelting mechanism responsible for sustaining channel growth is hampered by the increased resistance to flow. Isotherms for Case 2, Fig. 11(c), reveal intrusion of colder interdendritic fluid into the melt above each channel. However, thermal penetration is not as significant as that predicted for Case 1, Fig. 6(c). For the more permeable conditions of Case 1, fluid expelled by the four channels is drawn from the entire mushy zone, including portions along the bottom chilled surface. For Case 2, however, fluid feeding the five channels is from the warmest location within the mush (i.e. adjacent to the liquidus). Solutal conditions are also different for the two cases. Channels spanning nearly the entire length of the mush and short residence times for fluid moving within each channel yield large

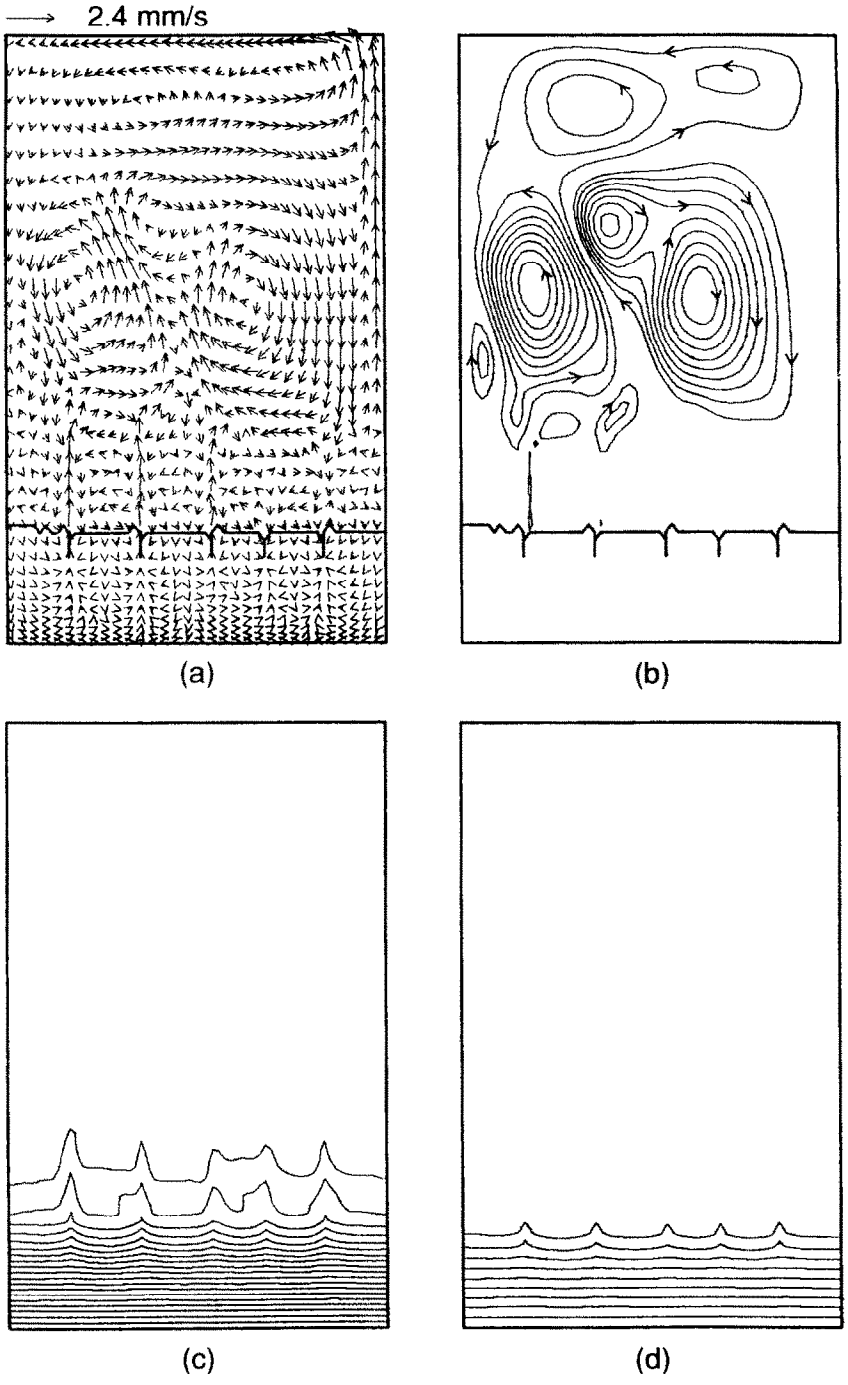


FIG. 11. Predicted solidification behavior at $t = 10$ min for Case 2: (a) velocity vectors ($|v_{max}| = 2.4$ mm s$^{-1}$); (b) streamlines; (c) isotherms ($T_{min} = -14°C$, $T_{max} = 50°C$); (d) liquid isocompositions ($f_{L,min}^{NH_4Cl} = 20\%$, $f_{L,max}^{NH_4Cl} = 32\%$).

solutal gradients at these sites for Case 1, Fig. 6(d). In contrast, the shallow channel penetration for Case 2 confines localized (non-horizontal) solutal gradients to the liquidus interface, Fig. 11(d).

Solidification conditions at $t = 19$ and 35 min, which may be compared with those of Case 1 (Figs. 8 and 9), are shown in Figs. 12 and 13, respectively. Details associated with phenomena at these and intermediate times (e.g. channel closings) are similar to those discussed for Case 1. It is noteworthy, however, that, at approximately $t = 24$ min, remelting of solid yielded a pocket of liquid at the base of the innermost channel. This pocket persisted until completion of the simulation, Fig. 13(d).

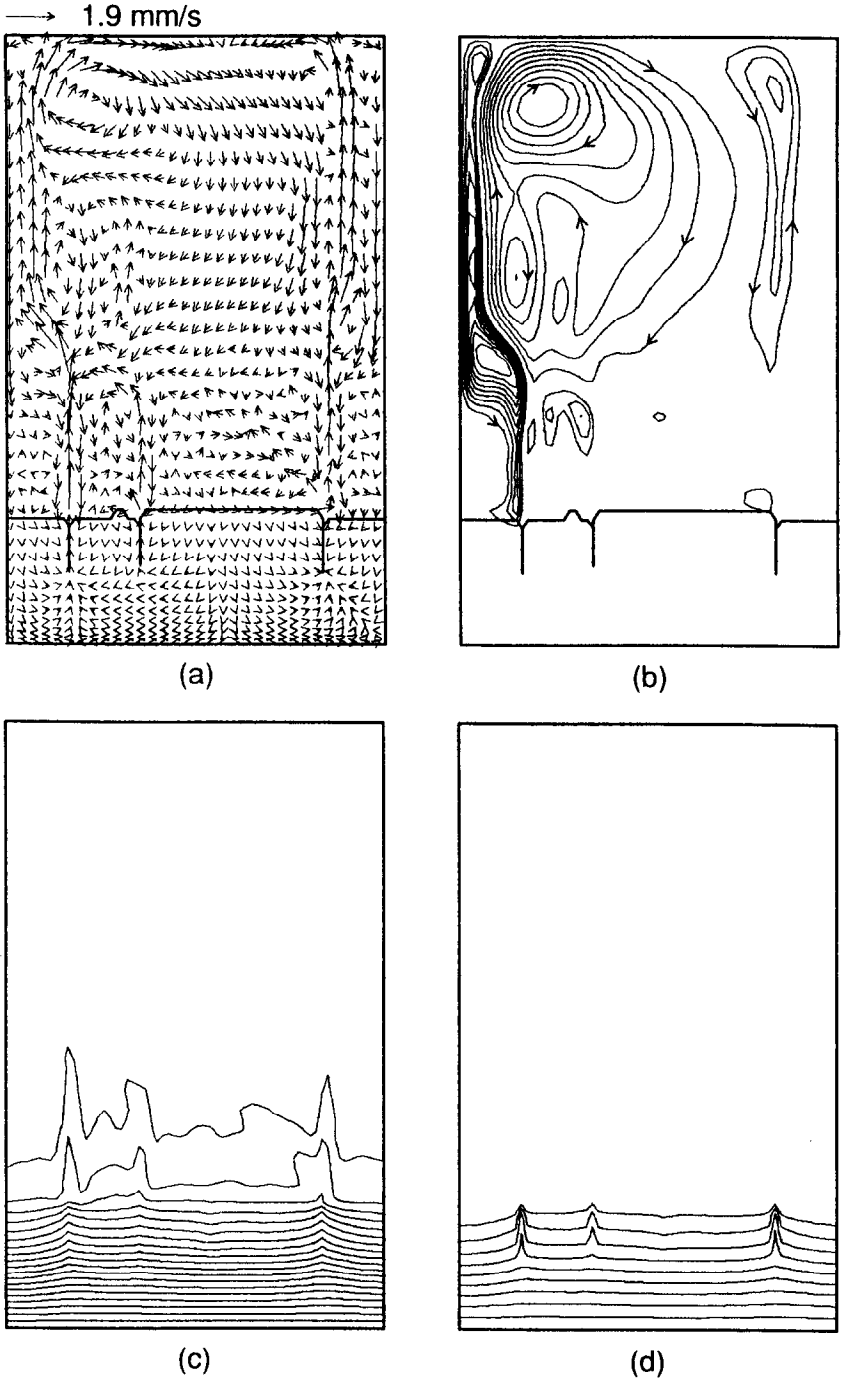


FIG. 12. Predicted solidification behavior at $t = 19$ min for Case 2: (a) velocity vectors ($|v_{max}| = 1.9$ mm $s^{-1}$); (b) streamlines; (c) isotherms ($T_{min} = -14°C$, $T_{max} = 48.7°C$); (d) liquid isocompositions ($f_{l,min}^{NH_4Cl} = 20\%$, $f_{l,max}^{NH_4Cl} = 31.8\%$).

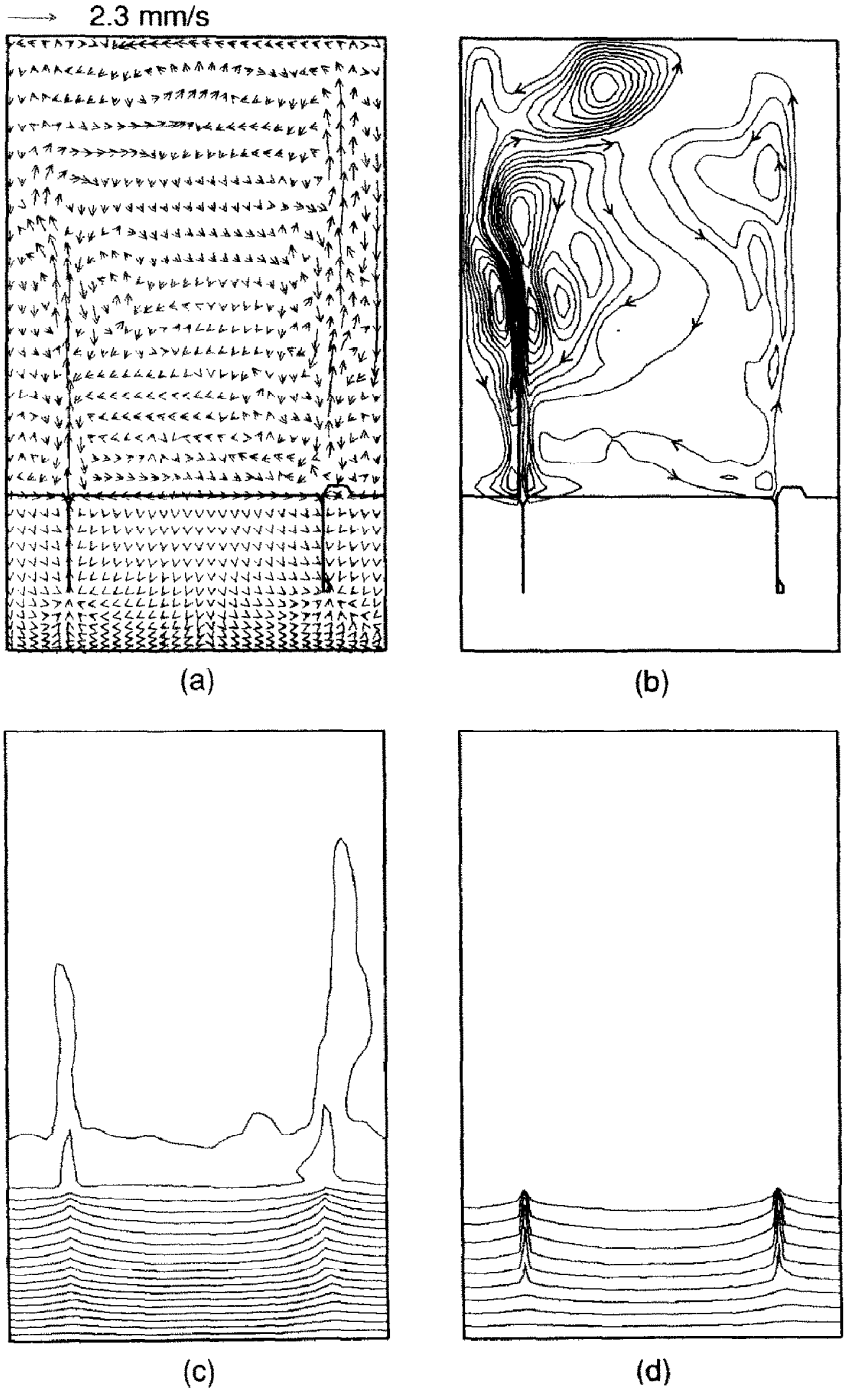


FIG. 13. Predicted solidification behavior at $t = 35$ min for Case 2: (a) velocity vectors ($|v_{max}| = 2.3$ mm s$^{-1}$); (b) streamlines; (c) isotherms ($T_{min} = -14$ C, $T_{max} = 45.3$ C); (d) liquid isocompositions ($f_{l,min}^{NH_4Cl} = 20\%$, $f_{l,max}^{NH_4Cl} = 31.2\%$).

## 4. CONCLUSIONS

To better understand the development of freckles (channel segregates) that often form in botton-chilled binary alloy castings, a numerical simulation of the solidification process has been performed. Because fluid motion induced by a density inversion within the mushy zone significantly influences solidification, a continuum formulation which readily accommodates advection of heat/mass was employed for the simulations. Solidification of an aqueous $NH_4Cl$ dendritic alloy was modelled.

Results from the numerical simulations revealed the manner in which channels develop. Namely, perturbations in primary field variables at the liquidus front induce highly localized permeability variations

that allow liquid to emerge from the mushy zone as buoyant plumes. The plumes are replenished by bulk liquid which *seeps* into the mush around a channel. Downward growth of each channel occurs as the result of a freezing point depression caused by solute-deficient fluid ascending within the channel. The predicted flow field in the bulk liquid, which is characterized by time dependent interactions between ascending plumes and adjoining cells, is qualitatively consistent with previous observations.

The sensitivity of predictions to the assumed permeability was addressed by considering two models based on different values of the dendritic arm spacing, which is a characteristic length scale of dendrite morphology. The simulation employing a more permeable mushy zone (Case 1) yielded enhanced channel formation and greater interaction between flows in the mushy region and the overlying melt. Predictions for Case 2, which was characterized by a smaller permeability and thus more viscous damping within the mushy zone, were less dynamic (i.e. less interaction between the bulk and mushy zone) and produced greater solid formation and liquidus front advancement.

The role of the bulk liquid in channel formation and evolution was found to be significant. In particular, model predictions have shown that entrainment of fluid from the melt into the mushy region is essential for channel development. This result suggests that, if the bulk liquid was perturbed in a manner that would inhibit fluid intrusion in the mushy zone, channel development would be curtailed. For instance, intermittent rotation during solidification would stir/agitate the bulk liquid, possibly disrupting fluid interchange between the melt and mushy regions and reducing freckle formation.

*Acknowledgements*—Support of this work has been provided by the U.S. Department of Energy under Award Number DE-FG02-87ER13759. The authors would like to express their appreciation to Mr Pat Prescott for many helpful comments and criticisms.

## REFERENCES

1. J. S. Turner, *Buoyancy Effects in Fluids*. Cambridge University Press, Cambridge (1973).
2. S. M. Copeley, A. F. Giamei, S. M. Johnson and M. F. Hornbecker, The origin of freckles in unidirectionally solidified castings, *Met. Trans.* **1**, 2193–2204 (1970).
3. T. D. McCay, M. H. McCay, S. A. Lowry and L. M. Smith, Convective instabilities during directional solidification, *J. Thermophys.* **3**(3), 345–350 (1989).
4. A. F. Giamei and B. H. Kear, On the nature of freckles in nickel base superalloys, *Met. Trans.* **1**, 2185–2192 (1970).
5. N. Streat and F. Weinberg, Macrosegregation during solidification resulting from density differences in the liquid, *Met. Trans.* **5**, 2539–2548 (1974).
6. L. Wang, V. Laxmanan and J. F. Wallace, Gravitational macrosegregation in unidirectionally solidified lead–tin alloy, *Met. Trans. A* **19A**, 2687–2694 (1988).
7. W. J. Boettinger, F. S. Biancaniello and S. R. Coriell, Solutal convection induced macrosegregation and the dendrite to composite transition in off-eutectic alloys, *Met. Trans. A* **12A**, 321–327 (1981).
8. A. Sample and A. Hellawell, The effect of mold precession on channel and macro-segregation in ammonium chloride–water analog castings, *Met. Trans. B* **13B**, 495–501 (1982).
9. A. K. Sample and A. Hellawell, The mechanisms of formation and prevention of channel segregation during alloy solidification, *Met. Trans. A* **15A**, 2163–2173 (1984).
10. J. R. Sarazin and A. Hellawell, Channel formation in Pb–Sn, Pb–Sb, and Pb–Sn–Sb alloy ingots and comparison with the system $NH_4Cl$–$H_2O$, *Met. Trans. A* **19A**, 1861–1871 (1988).
11. M. H. McCay and T. D. McCay, Experimental measurement of solutal layers in unidirectional solidification, *J. Thermophys.* **2**(3), 197–202 (1988).
12. D. R. Jenkins, Nonlinear analysis of convective and morphological instability during solidification of a dilute binary alloy, *PhysicoChem. Hydrodyn.* **6**(5/6), 521–537 (1985).
13. G. B. McFadden, R. G. Rehm, S. R. Coriell, W. Chuck and K. A. Morrish, Thermosolutal convection during dendritic solidification, *Met. Trans. A* **15A**, 2125–2137 (1984).
14. W. D. Bennon and F. P. Incropera, A continuum model for momentum, heat and species transport in binary solid–liquid phase change systems—I. Model formulation, *Int. J. Heat Mass Transfer* **30**, 2161–2171 (1987).
15. C. Beckermann and R. Viskanta, Double-diffusive convection during dendritic solidification of a binary mixture, *PhysicoChem. Hydrodyn.* **10**(2), 195–213 (1988).
16. M. C. Christenson, W. D. Bennon and F. P. Incropera, Solidification of an aqueous ammonium chloride solution in a rectangular cavity—II. Comparison of predicted and measured results, *Int. J. Heat Mass Transfer* **32**, 69–79 (1989).
17. W. D. Bennon and F. P. Incropera, The evolution of macrosegregation in statically cast binary ingots, *Met. Trans. B* **18B**, 611–616 (1987).
18. W. D. Bennon and F. P. Incropera, Numerical analysis of binary solid–liquid phase change using a continuum model, *Numer. Heat Transfer* **13**, 277–296 (1988).
19. S. Asai and I. Muchi, Theoretical analysis and model experiments on the formation mechanism of channel-type segregation, *Trans. ISIJ* **18**, 90–98 (1978).
20. S. V. Patankar, *Numerical Heat Transfer and Fluid Flow*. Hemisphere, Washington, DC (1980).
21. W. Bausch and W. Waidelich, On the thermal conductivity of ammonium- and deutero-ammonium chloride, *Phys. Lett.* **30A**, 190–191 (1969).
22. H. E. Huppert, The fluid mechanics of solidification, *J. Fluid Mech.* **212**, 209–240 (1990).

## SOLIDIFICATION UNIDIRECTIONNELLE D'UN ALLIAGE BINAIRE ET EFFETS DU MOUVEMENT FLUIDE INDUIT

**Résumé**—La solidification d'une substance binaire dans une géométrie refroidie par la base est simulée numériquement dans des conditions pour lesquelles une convection à large échelle résulte d'une inversion de densité, induite par la composition, dans la région de boue. Le modèle prédit avec succès les caractéristiques de la formation de la région boueuse qui a été déjà observée. La croissance commence au front de liquidus et, à cause de la dépression localisée du point de gel (fusion), se propage vers le bas. Les canaux agissent comme des parcours de moindre résistance pour le transport du fluide interdendritique dans le liquide. L'échappement du fluide hors de la zone boueuse forme des panaches à l'entrée de chaque canal et les panaches sont soutenus par la pénétration du liquide à travers le front du liquidus et une advection simultanée à travers les canaux. Les prédictions du développement du canal et de l'écoulement s'accordent bien avec les observations expérimentales antérieures.

## GERICHTETE ERSTARRUNG EINER ZWEISTOFFLEGIERUNG UND DER EINFLUSS EINER DABEI ENTSTEHENDEN FLUIDBEWEGUNG

**Zusammenfassung**—Die Erstarrung einer binären, von unten gekühlten Substanz wird numerisch für den Fall untersucht, daß es im Phasenwechselgebiet aufgrund einer konzentrationsbedingten Dichteinversion zu großräumiger Konvektion kommt. Das Modell ist in der Lage, die Ausbildung von Kanälen im Phasenwechselgebiet vorherzusagen, was bisher zwar beobachtet, aber noch nicht berechnet werden konnte. Die Kanäle beginnen an der Liquidusgrenze und schreiten aufgrund einer örtlichen Unterdrückung des Verfestigungspunktes zur Kühlplatte hin fort. Die Kanäle wirken als Wege des geringsten Widerstandes für den Fluidtransport zwischen den Dentriden hin zur überlagerten Flüssigkeitsmasse. Das aus der Phasenwechselzone austretende Fluid bildet an den Kanalenden Auftriebsblasen, die dadurch aufrecht erhalten werden, daß Flüssigkeit durch die Liquidusgrenze dringt und anschließend zu den Kanälen hinströmt. Die Berechnungen für die Ausbildung der Kanäle sowie für die Ausbildung der Strömung in der überlagerten Schmelze stimmen qualitativ mit früheren experimentellen Beobachtungen überein.

## ОДНОНАПРАВЛЕННОЕ ЗАТВЕРДЕВАНИЕ БИНАРНОГО СПЛАВА И ЭФФЕКТЫ ВЫНУЖДЕННОГО ДВИЖЕНИЯ ЖИДКОСТИ

**Аннотация**—Численно моделируется затвердевание бинарного вещества в геометрии с охлаждаемым основанием в условиях крупномасштабной конвекции, происходящей в результате обусловленной составом вещества инверсии плотности в пористой области. Результаты модельных испытаний позволяют успешно предсказывать характеристики процесса образования канала в пористой области, которые до сих пор не подлежали определению. Установлено, что рост канала начинается у фронта ликвидуса и, благодаря локализованному понижению точки замерзания (плавления), распространяется вниз в направлении охлаждаемой пластины. Каналы служат ходами наименьшего сопротивления для переноса междендритной жидкости в вышележащую объемную жидкость. Жидкость, покидающая пористую область, образует струи у входа в каждый канал, и эти струи поддерживаются проникновением объемной жидкости через фронт ликвидуса и послелующей адвекцией по направлению к каналам. Расчеты, полученные для развития каналов и течения в вышележащем расплаве, качественно согласуются с экспериментальными наблюдениями.